PHYSICAL REVIEW MATERIALS **7**, 114202 (2023)

Unraveling the complex electronic and topological landscape of triclinic enantiomorphic Nb P_xAs_{1-x} alloys through first-principles analysis

Samira Sadat Nourizadeh,[1] Aminollah Vaez,[1,*] and Daryoosh Vashaee[2,3,†]
[1] *Faculty of Physics, University of Isfahan, Isfahan 8174673441, Iran*
[2] *Department of Electrical and Computer Engineering, North Carolina State University, Raleigh, North Carolina 27606, USA*
[3] *Department of Materials Science and Engineering, North Carolina State University, Raleigh, North Carolina 27606, USA*

(Received 12 July 2023; accepted 17 October 2023; published 27 November 2023)

This paper undertakes a comprehensive examination of the electronic and topological properties of triclinic enantiomorphic Nb P_xAs_{1-x} alloys ($x = 0$, 0.25, 0.50, 0.75, 1) belonging to the space group $P1$, through first-principles and Wannier-based tight-binding analyses. Our paper reveals band inversion coupled with a distinctive fourfold band crossing near the Fermi energy, attributed to hybridization among Nb-d orbitals. Intriguingly, Nb P_xAs_{1-x} alloys exhibit nontrivial topological features even without spin-orbit coupling (SOC), primarily due to band inversion. Upon incorporating SOC, the fourfold band crossings transition into gapped bands, bifurcating into pairs of Weyl points with distinct chiralities. These Weyl points possess linear dispersion, categorizing the alloys as type-I topological Weyl semimetals. Additionally, SOC induces the emergence of Fermi arcs in the (111) surface states of the first Brillouin zone, connecting Weyl points of opposite chiralities. The findings establish Nb P_xAs_{1-x} alloys as promising candidates for applications in topological materials, while enriching the understanding of topological phases and their correlations with electronic structure.

DOI: 10.1103/PhysRevMaterials.7.114202

I. INTRODUCTION

The advent of theoretical predictions surrounding topological insulator (TI) phases has spurred rigorous investigations into various kinds of topological states [1–3]. Beyond the TI phases, a plethora of topological phases with energy gaps exist, such as integer quantum Hall systems [1,4] and topological crystalline insulators [5,6]. These systems possess distinctive surface or edge states, which manifest the topological characteristics intrinsic to these materials [7]. The ongoing investigation of TIs has unearthed a novel class of topological phases known as topological semimetals (TSMs) in the realm of condensed matter physics [8–12]. Topological Dirac semimetals (DSMs), topological nodal-line semimetals, and topological Weyl semimetals (WSMs) are subcategories within TSMs. All of these TSMs share a feature where the band gap vanishes at certain points in momentum space (k space), a phenomenon that arises due to the underlying topology in k space and is further characterized by symmetries within the first Brillouin zone (BZ). However, the degeneracies in TSMs are not necessarily confined to high-symmetry points in the first BZ, rendering the efficient and systematic discovery of TSMs a challenging endeavor.

Topological DSMs serve as a three-dimensional (3D) analog to graphene, characterized by fourfold degenerate Dirac points (DPs) [13,14]. These DPs stem from a linear dispersion relation and are protected by both time-reversal (TR) and inversion (I) symmetries [15]. Intriguingly, by breaking either the TR or I symmetries, topological DSMs can undergo phase transitions into different electronic phases, such as TIs, WSMs, axion insulators, and topological superconductors. This tunability makes them a versatile platform for studying diverse quasiparticle phenomena [15]. Nodal-line semimetals, another variant of TSMs, feature a band gap closure along a loop in k space [16,17]. The third variant, WSMs, is characterized by bulk valence and conduction bands that intersect at isolated Weyl points (WPs). In the vicinity of WPs, the bands exhibit nondegenerate three-dimensional Dirac cones. WSMs have exotic electronic properties, which can be approximately described by the Weyl equation at low energies [18,19]. In systems with spin-orbit coupling (SOC), the presence of both TR and I symmetries results in double-degenerate states according to the Kramers-Kronig theorem [20]. For WSMs to exist, either TR or I symmetry must be broken [21]. WPs always occur in pairs, with opposite chiralities, due to the protection afforded by the band structure topology [10]. Notable features of WSMs include bulk Weyl fermions, surface Fermi arcs, chiral anomalies, drum-head surface states, gaplessness in the bulk, and pairs of WPs. These exotic features contribute to a host of intriguing properties such as extraordinarily large or even negative magnetoresistance, chiral magnetic effects, high carrier mobility, light effective masses, nontrivial Berry phases, quantum anomalous Hall effects, and unusual quantum oscillations [22–24]. Such properties render WSMs promising candidates for future applications in electronics, spintronics, and quantum computing devices [25,26].

In the quest to find materials with WSM properties, a variety of compounds, including pyrochlore iridates [9], TI-based heterostructures [27], $HgCr_2Se_4$ [28], as well as noncentrosymmetric and nonmagnetic transition-metal

---

[*] Corresponding author: vaez@phys.ui.ac.ir

[†] Corresponding author: dvashae@ncsu.edu

monopnictides like NbAs and NbP [29–31], have been the subject of theoretical investigations, among others [32–36]. Recently, the topological landscape has been significantly expanded through the investigation of two-dimensional (2D) materials like TiNI monolayers, revealing the necessity of employing appropriate functionals for accurate topological predictions [37]. Additionally, strain engineering has emerged as a viable approach to control the topological states in materials such as Heusler compounds, offering a variety of phase transitions [38]. Furthermore, bialkali-metal bismuthides have been predicted with promising thermoelectric properties and nontrivial topological phases under hydrostatic pressure [39]. Mechanical properties have also gained attention, as exhibited by the bialkali-metal bismuthides Cs(Na, K)$_2$Bi, which showcase tunable elastic properties and potential applications in nanoscale devices [40]. The thermal and mechanical enhancements through intercalation, as demonstrated by MoB$_4$, mark another breakthrough in 2D materials [41]. Meanwhile, transition-metal dichalcogenides have been rigorously studied for their optoelectronic properties, revealing potential for technological applications in transparent conductor technology [42].

Building upon earlier investigations into ternary alloys as potential topological materials, which encompassed an incisive analysis of the electronic and topological properties of Ta P$_x$As$_{1-x}$ compounds, revealing them as Weyl semimetals with distinct characteristics under the influence of SOC [43], this paper extends the focus to Nb P$_x$As$_{1-x}$ alloys to unravel the complexities of their electronic and topological landscape. This paper leverages alloying to produce various alloys of NbP and NbAs, recognized for their WSM properties. The aim is to investigate the distinct electronic and topological traits of these alloys. This paper relies on first-principles calculations derived from density functional theory (DFT) [44] and the Wannier-based tight-binding (TB) method [45].

The subsequent sections of this paper are organized as follows: In Sec. II, we offer a concise description of the methods and computational tools employed in this research. Section III presents our calculation outcomes and delves into a discussion about these results. Finally, the salient points of this paper are summarized and concluded in Sec. IV.

II. COMPUTATIONAL METHODOLOGY

In this paper, the structural and electronic properties of the Nb P$_x$As$_{1-x}$ alloys (where $x = 0$, 0.25, 0.50, 0.75, 1) were investigated using DFT calculations employing the full potential linearized augmented plane wave (FP-LAPW) method as implemented in the WIEN2K code [46]. DFT is recognized as one of the most reliable methods for computing the electronic structure of solids [44]. The total energy calculations were conducted using the generalized gradient approximation parametrized by Perdew, Burke, and Ernzerhof, considering exchange and correlation effects with and without SOC [47].

In the FP-LAPW method, real space is partitioned into two regions: muffin-tin spheres and the interstitial region. Within the muffin-tin spheres, the wave function is expanded in terms of spherical harmonics up to a maximum angular momentum, $l_{\max}$, of 10. The wave function in the interstitial region is represented using plane waves with a cutoff, $K_{\max}$, defined as $K_{\max} = 10.0/R_{\mathrm{MT}}$ in atomic units, where R_{MT} is the smallest atomic muffin-tin radius for each alloy. The charge density and potential were expanded using a Fourier series truncated at $G_{\max} = 12.0\ \mathrm{Ry}^{1/2}$. Integration over the first BZ was performed using a $6\times6\times2$ k-point mesh for the triclinic alloys in the irreducible first BZ. Total energies were converged to within 10^{-5} eV.

To probe the topological properties, the Bloch wave function was projected onto the maximally localized Wannier functions (MLWF) [45]. The tight-binding model Hamiltonian parameters were ascertained from the MLWF overlap matrix and atomiclike Wannier functions corresponding to the Nb-5d, P-4p, and As-4p orbitals, utilizing the WANNIERTOOLS code. For the computation of topological properties and invariants such as chirality and surface states, the WANNIERTOOLS code was employed [48]. This code operates within the tight-binding framework, typically generated by software packages like WANNIER90 [49]. WANNIERTOOLS can categorize the topological phase of a material through the calculation of the Wilson loop [50]. Additionally, it computes the surface state spectrum, which can be experimentally discerned through angle-resolved photoemission spectroscopy [49,51] or scanning tunneling microscopy [52,53]. Utilizing the WANNIERTOOLS code, we were able to calculate the precise positions of the WPs and DPs, nodal line structures, Berry phase encircling a closed momentum loop, and Berry curvature within the first BZ [54–56].

III. RESULTS AND ANALYSIS

In Sec. IIIA, we present the structural and topological properties of the Nb P$_x$As$_{1-x}$ alloys (where $x = 0$, 0.25, 0.50, 0.75, 1) without considering the SOC. Subsequently, in Sec. IIIB, we incorporate the effects of SOC and analyze how this inclusion alters the structural and topological attributes of the Nb P$_x$As$_{1-x}$ alloys. Finally, in Sec. IIIC, we delve into the topological surface states of the alloys and discuss their implications.

This section is structured to systematically analyze the properties of the Nb P$_x$As$_{1-x}$ alloys, first by isolating the effect of SOC to understand the inherent structural and topological characteristics, followed by examining the influence of SOC on these properties. The culmination of this section with an analysis of the topological surface states provides comprehensive insights into the behavior and potential applications of these alloys.

A. Structural and topological characterization in the absence of spin-orbit coupling

The Nb P$_x$As$_{1-x}$ alloys crystallize in a triclinic enantiomorphic crystal structure, belonging to the space group $1P_1$ (no. 1), which notably lacks inversion symmetry.

The $1P_1$ space group is characterized by a unique property—an utter absence of any rotational axes, rotary-inversion axes, screw axes, or mirror planes [52,53]. Consequently, within the unit cell of the $1P_1$ space group, there is only one symmetry equivalent position. In order to simulate the crystal structure of the Nb P$_x$As$_{1-x}$ alloys, we constructed a $2\times2\times2$ supercell based on the structure of NbP. The

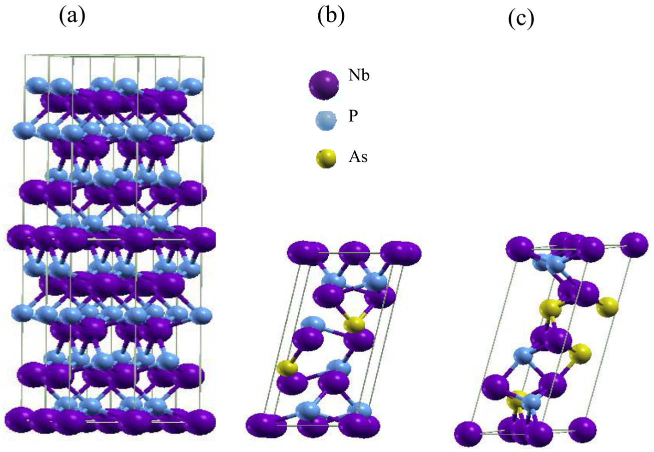

FIG. 1. Crystal structures of Nb P_xAs_{1-x} alloys. (a) The 2×2×2 supercell representation, which is constructed to simulate the varying concentrations of As in Nb P_xAs_{1-x} alloys. (b) The primitive unit cell adhering to the $1P_1$ space group in $NbP_{0.75}As_{0.25}$ alloy, emphasizing the triclinic enantiomorphic crystal structure inherent to these alloys. (c) The primitive unit cell adhering in $NbP_{0.5}As_{0.5}$ alloy.

phosphorus (P) atoms were then systematically replaced by arsenic (As) atoms to form various alloys with As concentrations of 25, 50, 75, and 100%. The supercell crystal structure of Nb P_xAs_{1-x} alloys is depicted in Fig. 1(a) and the primitive crystal structures for $NbP_{0.75}As_{0.25}$ and $NbP_{0.5}As_{0.5}$ alloys are depicted in Figs. 1(b) and 1(c), respectively.

In the initial stage of our computational analysis, we calculated the equilibrium lattice parameters of the Nb P_xAs_{1-x} alloys by minimizing the total energy E_t with respect to the volume. For this purpose, we employed the Birch-Murnaghan equation of state [9], and the optimized lattice parameters are presented in Table I.

The atomic positions of the Nb P_xAs_{1-x} alloys, with x ranging from 0 to 1, were subjected to relaxation, ensuring that the forces acting on each atom were reduced to below 1.0 mRy/a.u. following the relaxation process. One key aspect for evaluating the viability of a crystalline structure is its formation energy,E_f. The E_f per formula unit for these alloys, except NbP and NbAs, can be quantified through the expression

$$\begin{aligned} E_f(\mathrm{NbP}_x\mathrm{As}_{1-x}) &= E_t(\mathrm{NbP}_x\mathrm{As}_{1-x}) - xE_t(\mathrm{NbP}) \\ &\quad - (1-x)\,E_t(\mathrm{NbAs}). \end{aligned} \tag{1}$$

TABLE I. Summary of lattice constants (a and c), total energy (E_t), and formation energy (E_f) for Nb P_xAs_{1-x} alloys across different As concentrations.

	a(Å)	c(Å)	E_t (eV)	E_f (eV)
NbAs	4.840	12.157	–97305.944	–0.893
$NbPb_{0.25}As_{0.75}$	4.800	12.070	–89630.076	–0.018
$NbPb_{0.5}As_{0.5}$	4.758	11.981	–81954.172	–0.200
$NbPb_{0.75}As_{0.25}$	4.714	11.890	–74278.299	–0.014
NbP	4.685	11.845	–66602.398	–0.965

In this expression, $E_t(\mathrm{NbP}_x\mathrm{As}_{1-x})$, $E_t(\mathrm{NbP})$, and $E_t(\mathrm{NbAs})$ represent the E_t per formula unit for Nb P_xAs_{1-x}, NbP, and NbAs compounds, respectively. By utilizing this equation, the E_f of the Nb P_xAs_{1-x} alloys for various As concentrations was computed and is displayed in Table I. Notably, the E_fs for all concentrations are negative, signifying that these alloys are thermodynamically stable. The formation energy of NbP(As) is calculated by Eq. (2):

$$E_f[\mathrm{NbP(As)}] = E_t[\mathrm{NbP(As)}] - \frac{E_t(\mathrm{Nb})}{n} - \frac{E_t[\mathrm{P(As)}]}{n}, \tag{2}$$

where E_t(Nb) and E_t(P(As)) are the total energy of Nb or P(As), respectively, and n is the number of Nb or P(As) atoms in the primitive cells of NbP(As).

The electronic band structure is a critical concept in solid-state physics, underpinning the understanding of various electrical properties of crystalline materials. In this paper, the electronic band structures of the Nb P_xAs_{1-x} alloys, without considering the SOC, were computed along specific high-symmetry directions ($Z-S-S1-\Gamma-Z-N-M$) within the first Brillouin zone, as depicted in Fig. 4(a). The calculations encompassed an energy range of −4 to 4 eV and were performed at zero pressure. The resulting band structures are presented in Fig. 2, and provide insights into the electronic properties of these alloys and their potential applications.

To examine the origins of the computed band structure, both the total and atomic density of states (DOS) are illustrated in Fig. 2. The calculations for the total and atomic DOS employed a 6×6×2 k-point grid for all the alloys. It is worth noting that the individual DOS plots for Nb, P, and As represent the density of states for a single atom of the respective type. To reconcile with the total DOS, the reader should consider that our supercell consists of eight sites, each for Nb and for P (or As). Focusing on the regions surrounding the Fermi energy, it becomes evident that the Nb-5d orbital predominantly influences the distribution of the total DOS in all the alloys. As depicted in Fig. 2, the Nb P_xAs_{1-x} alloys for all values of x exhibit metallic characteristics. The bands following the $\Gamma-Z-M$ directions do not participate in charge transport, whereas those along the $Z-S-S1-\Gamma$ directions play a significant role in electrical conduction. Consequently, our analysis concentrates on the bands near the Fermi level along the $Z-S-S1-\Gamma$ trajectories. The intersections between the valence and conduction bands are in close proximity to the Fermi level and are highlighted by yellow boxes in Fig. 2. These intersection points exhibit linear dependence of energy on wave vectors near the crossing points. Multifold intersections can be observed at energies of 0.02 eV in the $S-S1$ directions.

The band crossings along the $Z-S-S1-\Gamma$ pathway primarily arise from band inversion. Within the $S-S1$ trajectory, the orbital-resolved bands' calculation displayed in Fig. 2(f) distinctly shows that the energy of the Nb$-dz^2$ orbital is inferior to that of the Nb-d_{xz} and d_{yz} orbitals, thereby creating an inverted band structure relative to the standard arrangement.

This particular band inversion within the $S-S1$ path suggests the possibility of nontrivial band topologies. Notably,

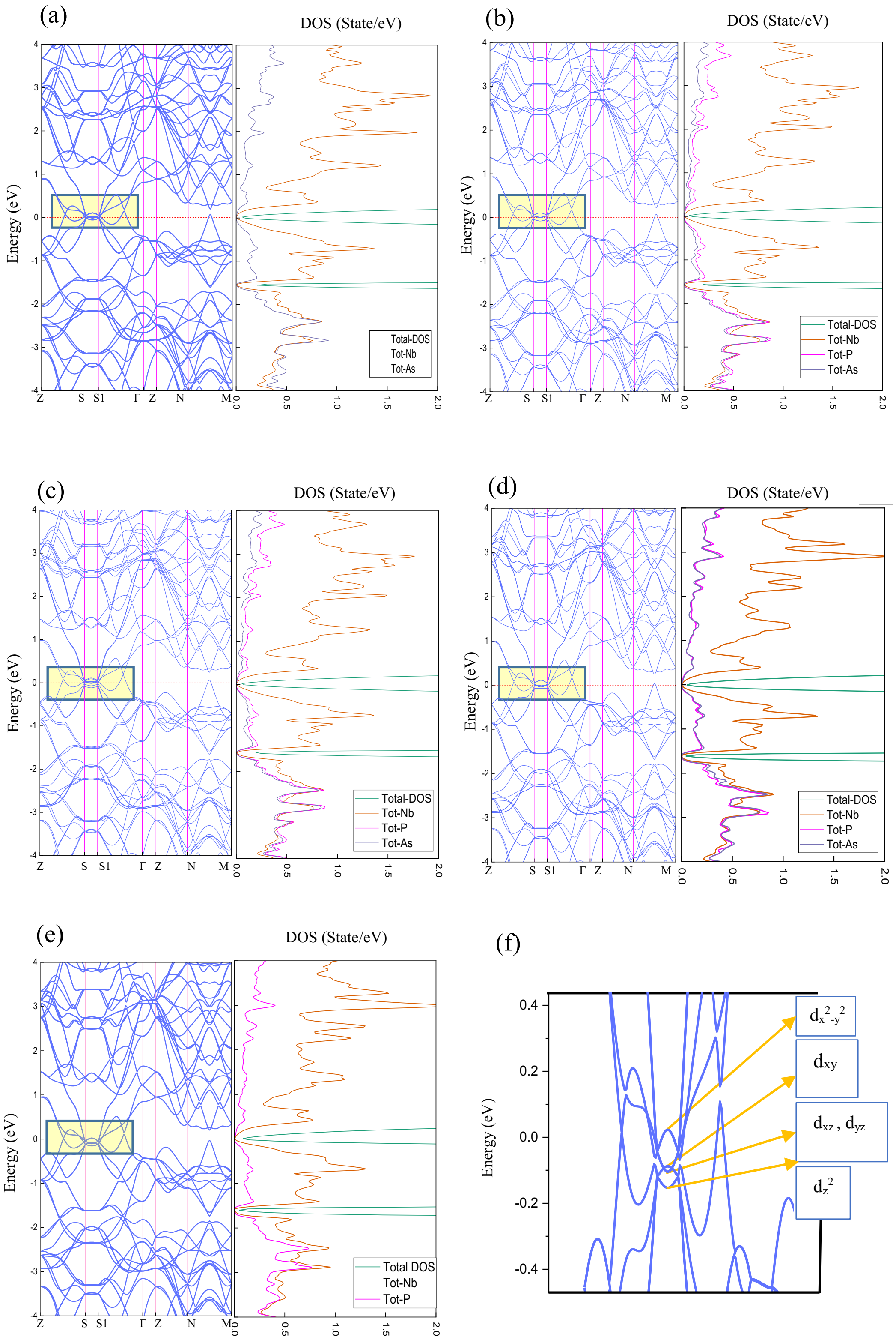

FIG. 2. Band structure and density of states (DOS) for the NbP_xAs_{1-x} alloys with varying concentrations of x (0, 0.25, 0.50, 0.75, 1) without considering spin-orbit coupling. (a)–(e) The band structure and DOS for x values of 0, 0.25, 0.50, 0.75, and 1, respectively. (f) The orbital-resolved band structure specific to NbP.

the band inversion observed in the $S-S1$ path is not attributed to SOC, unlike band inversions in certain topological nodal-line semimetals [17,54] and some TSMs [55]. The crossing bands at the S and $S1$ points comprise one double-degenerate band made up of the Nb-d_{z^2} and d_{xy} orbitals, and another double-degenerate band consisting of the d_{xz} and d_{yz} orbitals. These two crossing bands are associated with different irreducible representations, making the band crossing points

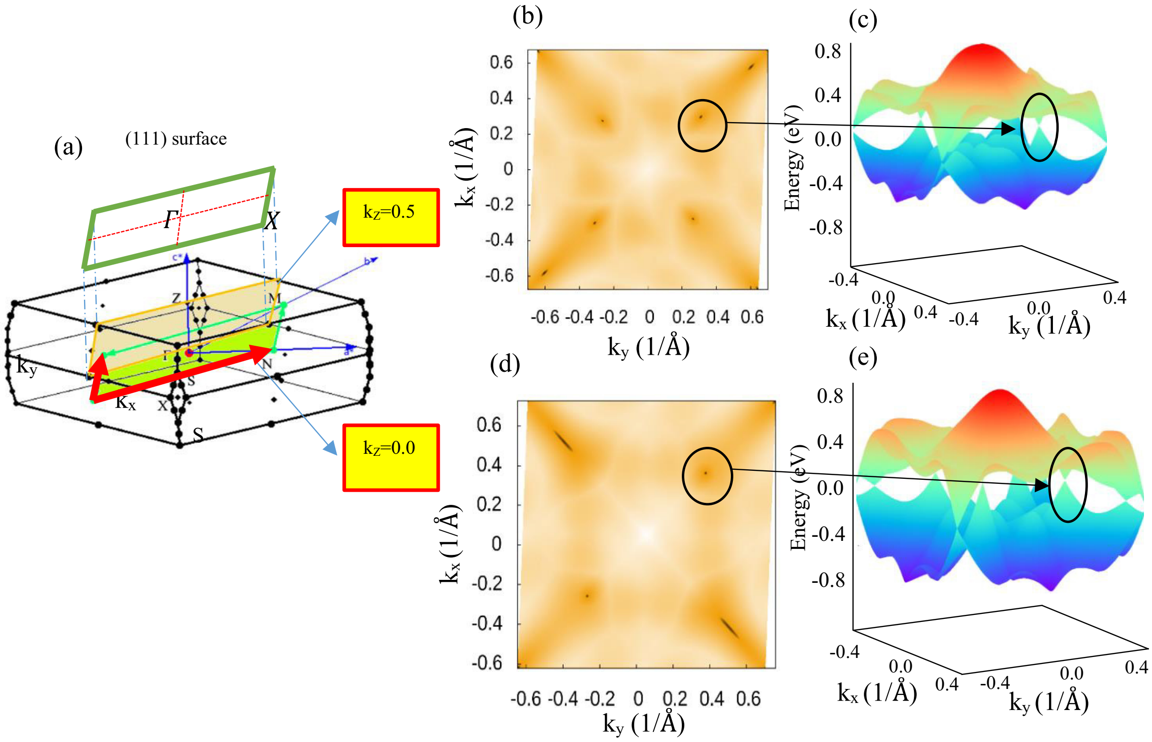

FIG. 3. (a) The first BZ of the triclinic structure and its (111) surface. (b), (c) The energy gap, $\Delta E(k_1,\ k_2)$, between the lowest conduction band and the highest valence band at $k_z = 0.5$ and 0, respectively, without considering SOC. (d), (e) The 3D band dispersion surrounding the crossing points for the NbP compound at $k_z = 0.5$ and 0, respectively, without SOC.

at the S and $S1$ points fourfold degenerate and safeguarded by time-reversal symmetry as well as space-group symmetry.

In addition to the S and $S1$ points, another location exists along the $Z-S$ path that exhibits a fourfold degeneracy. Consequently, there are three Dirac-like cones present along the $Z-S-S1-\Gamma$ path, as illustrated in Fig. 2. Since the $\mathrm{Nb\,P}_x\mathrm{As}_{1-x}$ alloys lack inversion symmetry and have a specific point group, traditional methods of parity and symmetry analysis are not applicable for elucidating their topological properties. However, evaluating the energy gap, denoted as $\Delta E(k_1,\ k_2)$, between the lowest conduction band and the highest valence band across various k planes can be employed as an alternative approach to investigate topological properties. This method has been implemented in the WANNIERTOOLS code.

Computations of the energy gap across different k planes, without considering SOC, were executed for the $\mathrm{Nb\,P}_x\mathrm{As}_{1-x}$ alloys in order to closely examine the locations of the Dirac-like cones. As an example, the positions of the Dirac-like cones on the $k_z = 0$ and 0.5 planes for the NbP compound were calculated and are depicted in Figs. 3(b) and 3(c). Additionally, the 3D band dispersion surrounding the Dirac-like cones on the $k_z = 0$ and 0.5 planes for the NbP compound is demonstrated in Figs. 3(d) and 3(e).

This analysis provides insight into the complex band structure and topological properties of the $\mathrm{Nb\,P}_x\mathrm{As}_{1-x}$ alloys. The presence of Dirac-like cones and their locations in the momentum space is essential in understanding the electronic properties of these materials and their potential applications in novel electronic devices leveraging topological properties.

B. Electronic structures and topological properties in the presence of spin-orbit coupling

Spin-orbit coupling can substantially modify the band structure of materials, particularly in systems containing heavy elements where relativistic effects are more pronounced. To investigate the influence of SOC on $\mathrm{Nb\,P}_x\mathrm{As}_{1-x}$ alloys, we have performed calculations of the DOS and the band structures incorporating the effects of SOC. The results are illustrated in Fig. 4.

Analyzing the vicinity of the Fermi energy, it becomes evident that the total DOS is primarily contributed by the Nb-5d orbital, akin to the scenario when SOC is not considered. However, the incorporation of SOC results in pivotal changes to the band structure. One of the critical consequences of including SOC is the lifting of spin degeneracy, which is a manifestation of the coupling between the spin and orbital angular momenta of the electrons. However, the band inversion remains resilient to the incorporation of SOC, indicating the robustness of this feature.

Further insights can be garnered by scrutinizing the band crossings. It is observed that the band crossings at the high-symmetry points S and $S1$ remain intact, while the crossings along the $Z-S$ and $S1-\Gamma$ directions open up to form gaps. Moreover, the fourfold degeneracy that was present at points S and $S1$ in the absence of SOC now resolves into two sets of doubly degenerate points. The splitting of degeneracies suggests the potential presence of topological phases in the alloys, necessitating further examination.

Additionally, a noteworthy observation is that some of the band crossings do not form gaps but rather undergo a

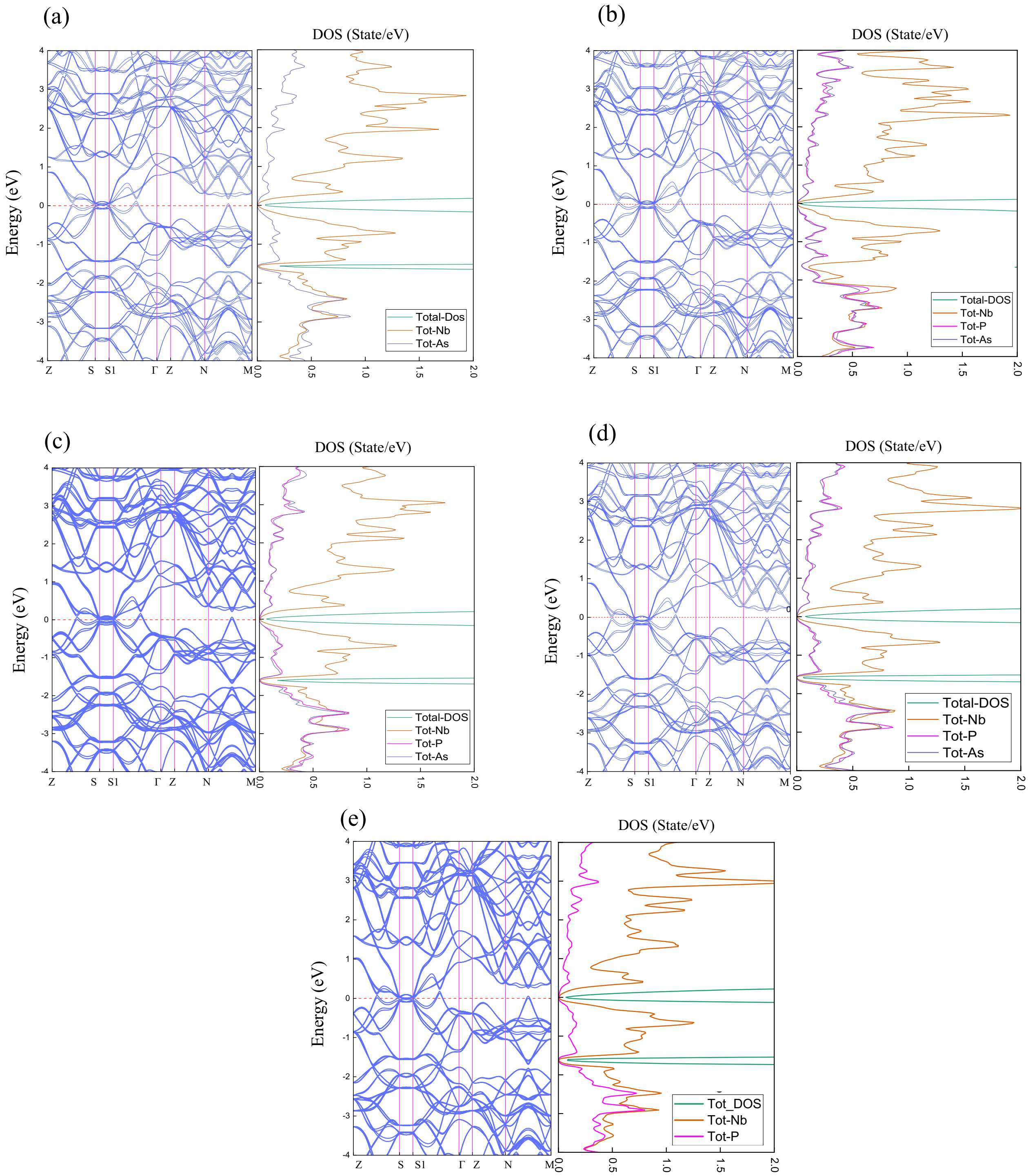

FIG. 4. Electronic band structure and DOS of the Nb P_xAs_{1-x} alloys, considering spin-orbit coupling, for different compositions: (a) $x = 0$, (b) $x = 0.25$, (c) $x = 0.50$, (d) $x = 0.75$, and (e) $x = 1$. This illustrates the evolution of the electronic properties with varying composition and the impact of SOC on the band structure.

splitting into WPs with a relative shift in momentum space. The precise positions of these WPs can be ascertained through a systematic search within the first BZ using Wannier-based TB bands, as implemented in the WANNIERTOOLS code. Employing a multidimensional minimization technique [56], the positions of the WPs are identified, following which the chirality associated with these points is determined. The chirality is instrumental in understanding the topological nature of the electronic bands and is associated with novel phenomena such as the chiral anomaly.

Therefore, the inclusion of SOC is essential to accurately describe the electronic and topological properties of Nb P_xAs_{1-x} alloys, particularly in capturing the lifting of spin degeneracy and the emergence of WPs.

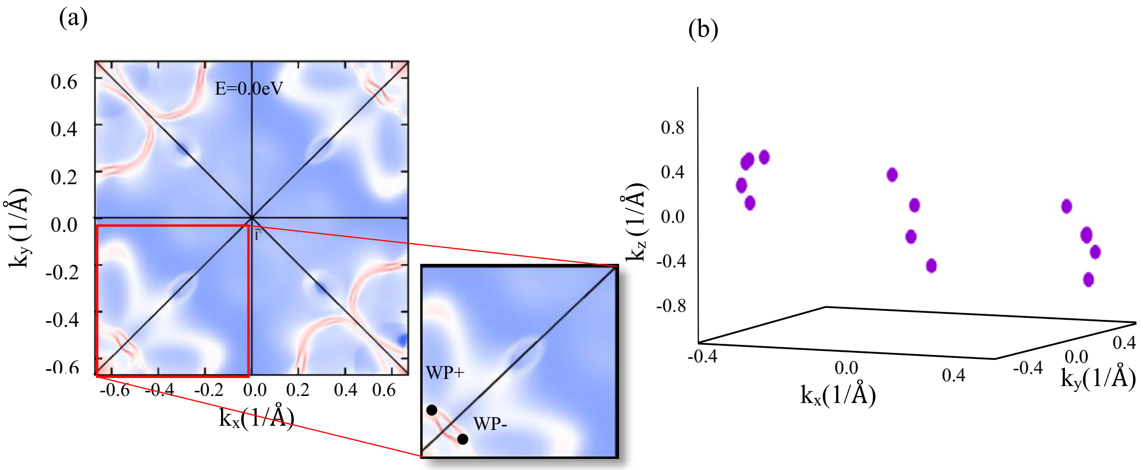

FIG. 5. (a) Surface state spectrum of the NbP compound considering SOC, plotted on the (111) surface of the first Brillouin zone, highlighting the emergence of Fermi arcs. The Fermi arcs with a zoomed-in view, connecting the WPs of opposite chirality, are shown. (b) Positioning of the WPs with SOC consideration for the NbP compound, which engender the Fermi arcs along the (111) surface of the first Brillouin zone.

The chirality of the WPs is a fundamental topological property that corresponds to the charge of a magnetic monopole in momentum space. This intrinsic characteristic can be quantified by calculating the integral over a closed two-dimensional surface encircling the Weyl point in k space. Following this methodology, the chiralities of the WPs in the Nb P_xAs_{1-x} alloys were computed and found to possess values of −1 and +1. These values serve to designate the WPs as either sources or sinks of Berry curvature, respectively. Moreover, a key topological constraint is that the net charge, or summed chirality, of all WPs within the first BZ must be conserved, amounting to zero. This constraint is intimately related to the underlying symmetries and topological invariants of the system.

In the context of the Nb P_xAs_{1-x} alloys, the Weyl cones exhibit characteristics consistent with type-I topological WSMs, reminiscent of the features observed in the TaAs family of materials which also possess broken inversion symmetry (see Supplemental Material [57]). It is vital to note that type-I WSMs are distinguished by the conservation of Lorentz symmetry and the proximity of the energy levels of the WPs to the Fermi level. This proximity has implications for the material's electronic properties, as it suggests that the exotic phenomena associated with WPs could be accessible at energies relevant for practical applications.

Therefore, the presence of WPs with distinct chiralities in Nb P_xAs_{1-x} alloys and their classification as type-I WSMs highlight the rich topological landscape and potential for novel electronic behavior in these materials.

C. Exploration of topological surface states

A hallmark characteristic of Weyl semimetals is the manifestation of surface Fermi arcs, which are novel surface states that arise due to the bulk-edge correspondence [7]. These Fermi arcs are obligated to initiate and terminate at the projection of two or more WPs that possess distinct chiralities on the surface Brillouin zone. In light of this, it is imperative to authenticate the presence of these exotic surface states in the Nb P_xAs_{1-x} alloys. To accomplish this, we computed the surface state spectra on the (111) surface of the BZ using the iterative Green's function method, as executed in the WANNIERTOOLS code. We observed that the (111) surface state spectra for all Nb P_xAs_{1-x} alloys were remarkably similar, and as such, we elected to present only the (111) surface state spectrum for the NbP alloy as a representative case in Fig. 5(a).

In Fig. 5(a), the spectral weight of certain bulk bands in proximity to the surface state is depicted in blue and white regions, whereas the dark red curves exclusively represent the surface state. Intriguingly, Fermi arcs are discernible in the surface state spectrum, bridging the WPs. The k-space positions of the WPs for the NbP compound were systematically determined and are illustrated in Fig. 5(b). The k-space positions of the WPs for the Nb P_xAs_{1-x} alloys with $x = 0$, 0.25, 0.50, 0.75 are also investigated and demonstrated [57]. A close inspection of Figs. 5(a) and 5(b) reveals that the k-space coordinates at which the surface Fermi arcs terminate coincide with the projection of the WPs onto the surface of the first BZ. It is noteworthy, however, that the (111) projection points with antipodal chiral WPs exhibit complete overlap, culminating in convoluted Fermi arcs. The structure and connectivity patterns of these arcs in the Nb P_xAs_{1-x} alloys are multifaceted, bearing resemblance to the complex characteristics observed in the TaAs family [58]. This intricate architecture underscores the nontrivial topological nature of the investigated alloys.

IV. CONCLUSIONS

This paper systematically investigated the structural, electronic, and topological properties of Nb P_xAs_{1-x} alloys for various concentrations ($x = 0$, 0.25, 0.50, 0.75, 1). The alloys were found to be thermodynamically stable and their electronic band structures were primarily governed by Nb-$5d$ orbitals around the Fermi level. Without SOC, the alloys exhibited band inversion and multifold band crossings, indicating possible nontrivial topological properties. When SOC was incorporated, the spin degeneracy was lifted while band inversion remained intact. Furthermore, WPs exhibiting linear dispersion were observed within the first BZ, classifying the alloys as type-I topological WSM in the same vein as the TaAs family. Additionally, the surface state spectrum revealed the existence of Fermi arcs on the (111) surface states, which connect the projected WPs in the first BZ. These Fermi arcs displayed complex patterns and connections with WPs and are indicative of the bulk-edge correspondence, characteristic of topological Weyl semimetals. These findings position Nb P_xAs_{1-x} alloys as promising candidates for further studies in topological materials science and possible applications in quantum computing and spintronics.

---

[1] C. L. Kane and E. J. Mele, Quantum spin Hall effect in graphene, Phys. Rev. Lett. **95**, 226801 (2005).

[2] C. L. Kane and E. J. Mele, Z_2 topological order and the quantum spin Hall effect, Phys. Rev. Lett. **95**, 146802 (2005).

[3] X. L. Qi, T. L. Hughes, and S. C. Zhang, Topological field theory of time-reversal invariant insulators, Phys. Rev. B **78**, 195424 (2008).

[4] Z. Fang, N. Nagaosa, K. S. Takahashi, A. Asamitsu, R. Mathieu, T. Ogasawara, H. Yamada, M. Kawasaki, Y. Tokura, and K. Terakura, The anomalous Hall effect and magnetic monopoles in momentum space, Science **302**, 92 (2003).

[5] Y. Tanaka, Z. Ren, T. Sato, K. Nakayama, S. Souma, T. Takahashi, K. Segawa, and Y. Ando, Experimental realization of a topological crystalline insulator in SnTe, Nat. Phys. **8**, 800 (2012).

[6] L. Fu, Topological crystalline insulators, Phys. Rev. Lett. **106**, 106802 (2011).

[7] G. M. Graf and M. Porta, Bulk-edge correspondence for two-dimensional topological insulators, Commun. Math. Phys. **324**, 851 (2013).

[8] A. Burkov and L. Balents, Weyl semimetal in a topological insulator multilayer, Phys. Rev. Lett. **107**, 127205 (2011).

[9] X. Wan, A. M. Turner, A. Vishwanath, and S. Y. Savrasov, Topological semimetal and Fermi-arc surface states in the electronic structure of pyrochlore iridates, Phys. Rev. B **83**, 205101 (2011).

[10] B. Yan and C. Felser, Topological materials: Weyl semimetals, Annu. Rev. Condens. Matter Phys. **8**, 337 (2017).

[11] H. Gao, J. W. Venderbos, Y. Kim, and A. M. Rappe, Topological semimetals from first principles, Annu. Rev. Mater. Res. **49**, 153 (2019).

[12] M. M. H. Polash, S. Yalameha, H. Zhou, K. Ahadi, Z. Nourbakhsh, and D. Vashaee, Topological quantum matter to topological phase conversion: Fundamentals, materials, physical systems for phase conversions, and device applications, Mate. Sci. Eng. R **145**, 100620 (2021).

[13] Z. Wang, Y. Sun, X. Q. Chen, C. Franchini, G. Xu, H. Weng, X. Dai, and Z. Fang, Dirac semimetal and topological phase transitions in A_3Bi (A = Na, K, Rb), Phys. Rev. B **85**, 195320 (2012).

[14] Z. Liu, J. Jiang, B. Zhou, Z. Wang, Y. Zhang, H. Weng, D. Prabhakaran, S. K. Mo, H. Peng, and P. Dudin, A stable three-dimensional topological Dirac semimetal Cd_3As_2, Nat. Mater. **13**, 677 (2014).

[15] Z. Liu, B. Zhou, Y. Zhang, Z. Wang, H. Weng, D. Prabhakaran, S. K. Mo, Z. Shen, Z. Fang, and X. Dai, Discovery of a three-dimensional topological Dirac semimetal, Na_3Bi, Science **343**, 864 (2014).

[16] C. Fang, H. Weng, X. Dai, and Z. Fang, Topological nodal line semimetals, Chin. Phys. B **25**, 117106 (2016).

[17] R. Yu, Z. Fang, X. Dai, and H. Weng, Topological nodal line semimetals predicted from first-principles calculations, Front. Phys. **12**, 127202 (2017).

[18] H. Weyl, Elektron und gravitation. I, Z. Phys. **56**, 330 (1929).

[19] S. F. Zhang, C. W. Zhang, P. J. Wang, and Q. F. Sun, Low-energy electronic properties of a Weyl semimetal quantum dot, Sci. China: Phys. Mech. Astron. **61**, 117811 (2018).

[20] A. Zyuzin, S. Wu, and A. Burkov, Weyl semimetal with broken time reversal and inversion symmetries, Phys. Rev. B **85**, 165110 (2012).

[21] N. Armitage, E. Mele, and A. Vishwanath, Weyl and Dirac semimetals in three-dimensional solids, Rev. Mod. Phys. **90**, 015001 (2018).

[22] H. Li, H. He, H. Z. Lu, H. Zhang, H. Liu, R. Ma, Z. Fan, S. Q. Shen, and J. Wang, Negative magnetoresistance in dirac semimetal Cd_3As_2, Nat. Commun. **7**, 10301 (2016).

[23] Y. Zhang, Y. Sun, and B. Yan, Berry curvature dipole in Weyl semimetal materials: An *ab initio* study, Phys. Rev. B **97**, 041101(R) (2018).

[24] J. Y. Wu, W. P. Su, and G. Gumbs, Anomalous magneto-transport properties of bilayer phosphorene, Sci. Rep. **10**, 7674 (2020).

[25] X. Wang and M. Zhang, Layered topological semimetals for spintronics, in *Spintronic 2D Materials* (Elsevier, Amsterdam, 2020), p. 273.

[26] X. Liu, C. Yue, S. V. Erohin, Y. Zhu, A. Joshy, J. Liu, A. M. Sanchez, D. Graf, P. B. Sorokin, and Z. Mao, Quantum transport of the 2D surface state in a nonsymmorphic semimetal, Nano Lett. **21**, 4887 (2021).

[27] T. V. Menshchikova, M. Otrokov, S. Tsirkin, D. Samorokov, V. Bebneva, A. Ernst, V. Kuznetsov, and E. V. Chulkov, Band structure engineering in topological insulator based heterostructures, Nano Lett. **13**, 6064 (2013).

[28] G. Xu, H. Weng, Z. Wang, X. Dai, and Z. Fang, Chern semimetal and the quantized anomalous Hall effect in HgCr 2 Se 4, Phys. Rev. Lett. **107**, 186806 (2011).

[29] S. M. Huang, S. Y. Xu, I. Belopolski, C. C. Lee, G. Chang, B. Wang, N. Alidoust, G. Bian, M. Neupane, and C. Zhang, A Weyl Fermion semimetal with surface Fermi arcs in the transition metal monopnictide TaAs class, Nat. Commun. **6**, 7373 (2015).

[30] X. Huang, L. Zhao, Y. Long, P. Wang, D. Chen, Z. Yang, H. Liang, M. Xue, H. Weng, Z. Fang, X. Dai, and G. Chen, Observation of the chiral-anomaly-induced negative magnetoresistance in 3D Weyl semimetal TaAs, Phys. Rev. X **5**, 031023 (2015).

[31] B. Lv, H. Weng, B. Fu, X. P. Wang, H. Miao, J. Ma, P. Richard, X. Huang, L. Zhao, and G. Chen, Experimental discovery of Weyl semimetal TaAs, Phys. Rev. X **5**, 031013 (2015).

[32] I. Belopolski, P. Yu, D. S. Sanchez, Y. Ishida, T. R. Chang, S. S. Zhang, S. Y. Xu, H. Zheng, G. Chang, and G. Bian, Signatures of a time-reversal symmetric Weyl semimetal with only four Weyl points, Nat. Commun. **8**, 942 (2017).

[33] H. Huang, K. H. Jin, and F. Liu, Alloy engineering of topological semimetal phase transition in Mg $Ta_{2-x}Nb_xN_3$, Phys. Rev. Lett. **120**, 136403 (2018).

[34] S. Jia, S. Y. Xu, and M. Z. Hasan, Weyl semimetals, Fermi arcs and chiral anomalies, Nat. Mater. **15**, 1140 (2016).

[35] P. F. Liu, J. Li, X. H. Tu, H. Li, J. Zhang, P. Zhang, Q. Gao, and B. T. Wang, First-principles prediction of ideal type-II Weyl phonons in wurtzite ZnSe, Phys. Rev. B **103**, 094306 (2021).

[36] D. S. Sanchez, G. Chang, I. Belopolski, H. Lu, J. X. Yin, N. Alidoust, X. Xu, T. A. Cochran, X. Zhang, Y. Bian, and S. S. Zhang, Observation of Weyl fermions in a magnetic noncentrosymmetric crystal, Nat. Commun. **11**, 3356 (2020).

[37] S. Yalameha, Z. Nourbakhsh, M. S. Bahramy, and D. Vashaee, New insights into band inversion and topological phase of TiNI monolayer, Phys. Chem. Chem. Phys. **25**, 12182 (2023).

[38] S. Yalameha, Z. Nourbakhsh, A. Ramazani, and D. Vashaee, Highly stable full Heusler order $Cs(Na, K)_2Bi$ with diverse topological phases controlled by strain engineering, Mater. Sci. Eng. B **273**, 115430 (2021).

[39] S. Yalameha, Z. Nourbakhsh, and D. Vashaee, Topological phase and thermoelectric properties of bialkali bismuthide compounds $(Na, K)_2RbBi$ from first-principles, J. Phys: Condens. Matter **34**, 105702 (2021).

[40] S. Yalameha, Z. Nourbakhsh, A. Ramazani, and D. Vashaee, Promising bialkali bismuthides $Cs(Na, K)_2Bi$ for high-performance nanoscale electromechanical devices: Prediction of mechanical and anisotropic elastic properties under hydrostatic tension and compression and tunable auxetic properties, Nanomaterials **11**, 2739 (2021).

[41] M. Alidoosti, D. N. Esfahani, S. Yalameha, and D. Vashaee, Unlocking the potential of hexagonal boron sheets: Giant improvements in thermal conductivity and mechanics through molybdenum intercalation, Mater. Today Phys. **32**, 101012 (2023).

[42] Y. Fazeli, Z. Etesami, Z. Nourbakhsh, and D. Vashaee, Unveiling the properties of transition-metal dichalcogenides: A comprehensive study of WTe2, WSe2, ZrTe2, and NiTe2 in bulk and monolayer forms, J. Mater. Sci. **58**, 10023 (2023).

[43] S. S. Nourizadeh, A. Vaez, and D. Vashaee, Emerging Weyl semimetal states in ternary Ta P_xAs_{1-x} alloys: Insights from electronic and topological analysis, Adv. Quantum Technol. **6**, 2300072 (2023).

[44] P. Hohenberg and W. Kohn, Density functional theory (DFT), Phys. Rev. **136**, B864 (1964).

[45] N. Marzari, A. A. Mostofi, J. R. Yates, I. Souza, and D. Vanderbilt, Maximally localized Wannier functions: Theory and applications, Rev. Mod. Phys. **84**, 1419 (2012).

[46] P. Blaha, K. Schwarz, F. Tran, R. Laskowski, G. K. Madsen, and L. D. Marks, WIEN2k: An APW + lo program for calculating the properties of solids, J. Chem. Phys. **152**, 074101 (2020).

[47] J. P. Perdew, K. Burke, and M. Ernzerhof, Generalized gradient approximation made simple, Phys. Rev. Lett. **77**, 3865 (1996).

[48] A. A. Mostofi, J. R. Yates, G. Pizzi, Y. S. Lee, I. Souza, D. Vanderbilt, and N. Marzari, An updated version of WANNIER90: A tool for obtaining maximally-localised Wannier functions, Comput. Phys. Commun. **185**, 2309 (2014).

[49] X. Zhang, L. Jin, X. Dai, and G. Liu, Topological type-II nodal line semimetal and Dirac semimetal state in stable kagome compound Mg_3Bi_2, J. Phys. Chem. Lett. **8**, 4814 (2017).

[50] Y. J. Hao, P. Liu, Y. Feng, X. M. Ma, E. F. Schwier, M. Arita, S. Kumar, C. Hu, M. Zeng, Y. Wang, and Z. Hao, Gapless surface Dirac cone in antiferromagnetic topological insulator $MnBi_2Te_4$, Phys. Rev. X **9**, 041038(2019).

[51] Z. Wang, K. Luo, J. Zhao, and R. Yu, Large Fermi arc and robust Weyl semimetal phase in Ag_2S, Phys. Rev. B **100**, 205117 (2019).

[52] W. M. Meier, C. A. Taylor, and U. O. Wales, *Space Group Patterns* (University College Cardiff, Cardiff, Wales, 1984).

[53] D. J. Fishek, Crystal classification and symbolism, Am. Mineral.: J. Earth Planet. Mater. **20**, 292 (1935).

[54] H. Huang, J. Liu, D. Vanderbilt, and W. Duan, Topological nodal-line semimetals in alkaline-earth stannides, germanides, and silicides, Phys. Rev. B **93**, 201114(R) (2016).

[55] I. Y. Sklyadneva, I. P. Rusinov, R. Heid, K. P. Bohnen, P. M. Echenique, and E. V. Chulkov, Pressure-induced topological phases of KNa_2Bi, Sci. Rep. **6**, 24137 (2016).

[56] A. S. Goryachih and M. A. Rachinskaya, Multidimensional global optimization method using numerically calculated derivatives, Proc. Comput. Sci. **119**, 90 (2017).

[57] See Supplemental Material at http://link.aps.org/supplemental/10.1103/PhysRevMaterials.7.114202 for calculated Weyl points coordination of Nb P_xAs_{1-x} alloys.

[58] H. Weng, C. Fang, Z. Fang, B. A. Bernevig, and X. Dai, Weyl semimetal phase in noncentrosymmetric transition-metal monophosphides, Phys. Rev. X **5**, 011029 (2015).